Letters

High-Order Frequency-Locked Loops: A Critical Analysis

Saeed Golestan, Josep M. Guerrero, and Juan. C. Vasquez

***Abstract*—In very recent years, some attempts for designing high-order frequency-locked loops (FLLs) have been made. Nevertheless, the advantages and disadvantages of these structures, particularly in comparison with a standard FLL and high-order phase-locked loops (PLLs), are rather unclear. This lack of knowledge is attributable to the difficulty of small-signal modeling of these high-order FLLs, which has limited their analysis to numerical studies. Focusing on three-phase FLLs, the idea of designing high-order FLLs is first generalized in this letter. Then, a second-order FLL is considered as the case study, and its small-signal modeling, stability analysis, and parameter tuning are presented. Finally, to gain insight about advantages and disadvantages of high-order FLLs, a theoretical and experimental performance comparison between the designed second-order FLL and a standard FLL (first-order FLL) as well as a unification between FLLs and PLLs is presented.**

***Index Terms*—Complex filters, frequency-locked loop (FLL), phase-locked loop (PLL), synchronization.**

I. Introduction

THE closed-loop synchronization techniques can be broadly classified into two major categories: phase-locked loops (PLLs) and frequency-locked loops (FLLs) [1]. In their standard structures, both PLLs and FLLs have a limited filtering capability. To deal with this problem, many efforts have been made by different researchers. The majority of these efforts have been concentrated on PLLs, and a little work has been conducted on FLLs. The reason behind this probably lies in the reference frame in which PLLs and FLLs are implemented. The PLLs are implemented in the synchronous reference frame. Therefore, their filtering capability can easily and effectively be improved by including additional low-pass filters (LPFs) and/or notch filters into their structure [2]. The FLLs, however, are realized in the stationary reference frame using generalized integrators [3]–[5] or complex bandpass filters (CBFs) [6]–[8]. Consequently, designing additional filters for incorporating into their structure is more difficult.

To enhance the filtering capability of FLLs, some attempts for designing high-order FLLs have been made in recent years. In [3], the parallel connection of multiple second-order generalized integrator-based quadrature signal generators (SOGI-QSGs) is suggested. These SOGI-QSGs work in a collaborative way, each of which is responsible for detecting a particular harmonic/disturbance component. This strategy is mainly interesting for applications where the selective extraction/rejection of harmonics is required. Following the same idea as in [3], the parallel configuration of multiple CBFs for implementing high-order three-phase FLLs is suggested in [6] and [8]. In [4], the series connection of two or more SOGI-QSGs is recommended. In this way, all possible harmonics, interharmonics, and noises in the grid voltage are considerably attenuated. In [5], it is shown that the SOGI-QSG can be seen as a first-order LPF, in which the integrator is replaced by the SOGI. Based on this perspective, a second-order SOGI-QSG is suggested in [5] and [9], which is implemented by replacing two integrators of a second-order LPF by two SOGIs. This second-order SOGI-QSG provides a higher filtering capability than the standard SOGI-QSG. The same idea is used in [9] for implementing a second-order CBF.

The main aim of this letter is to analyze the advantages and disadvantages of high-order FLLs. To this end, a general approach for implementing high-order CBF-based FLLs is first presented. This generalization should be considered as an extension of the work in [5] and [9]. Then, a second-order CBF-based FLL (briefly called the CBF-FLL2) is considered as the case study, and its small-signal modeling, stability analysis, and parameter tuning are presented. To the best of authors' knowledge, the small-signal modeling and stability analysis of high-order FLLs have not been presented before. Under a fair condition, a performance comparison between the CBF-FLL2 and a standard FLL is conducted, which provides a useful insight into the advantages and disadvantages of high-order FLLs. A unification between FLLs and PLLs is also provided.

II. Implementing High-Order FLLs

In the signal-processing theory, it is well known that a CBF can be realized by shifting the frequency response of an LPF [9]–[11]. In other words, an n-order CBF with the center frequency at ω_g can be obtained by replacing s in the transfer function of an n-order LPF with $s - jw_g$, as expressed in (1) and (2), where a_i $(i = 1, 2, \ldots, n)$ is the LPF coefficient. Eq. (1) and (2) are shown at the bottom of the next page. Notice that the complex operator j in (2) denotes a cross-coupling between two orthogonal axes, here α and β axes.

Manuscript received August 29, 2016; revised November 17, 2016; accepted November 23, 2016. Date of publication December 7, 2016; date of current version February 2, 2017.

The authors are with the Department of Energy Technology, Aalborg University, DK-9220 Aalborg, Denmark (e-mail: sgd@et.aau.dk; joz@et.aau.dk; juq@et.aau.dk).

Color versions of one or more of the figures in this letter are available online at http://ieeexplore.ieee.org.

Digital Object Identifier 10.1109/TPEL.2016.2636746

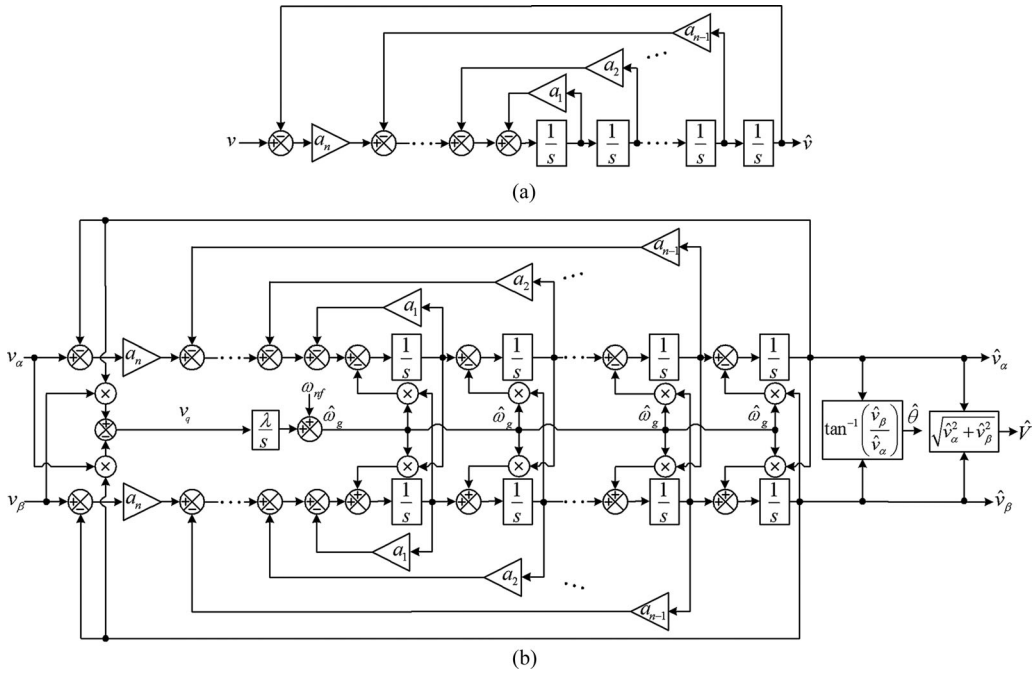

Fig. 1. (a) n-order LPF. (b) n-order CBF-based FLL.

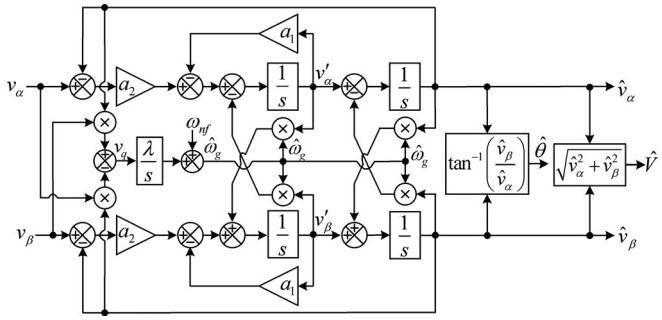

Fig. 2. Schematic diagram of the CBF-FLL2.

Based on the transfer function (1), the block diagram of the n-order LPF can be obtained, as shown in Fig. 1(a). Considering this diagram and the relation between the n-order CBF and LPF [see (1) and (2)], an n-order CBF-based FLL can be implemented, as shown in Fig. 1(b). Note that the frequency estimator in this structure is exactly the same as that in a standard three-phase FLL [2], [7]. Note also that the inverse tangent is calculated using a four-quadrant inverse tangent function.

III. Design Example: Second-Order CBF-FLL

Here, for the sake of brevity, a CBF-FLL2 is considered and analyzed. The schematic diagram of the CBF-FLL2 can be observed in Fig. 2. An alternative implementation of a second-order CBF can be found in [9]. In what follows, the small-signal modeling, stability analysis, and tuning procedure of the CBF-FLL2 are presented and discussed. It is worth mentioning that a similar procedure is applicable to an n-order CBF-based FLL.

A. Small-Signal Modeling

Throughout the modeling procedure, the input signals of the CBF-FLL2 are considered as

$$\begin{aligned} v_\alpha(t) &= V\cos(\theta) \\ v_\beta(t) &= V\sin(\theta) \end{aligned} \tag{3}$$

where V and $\theta = \int \omega_g dt$ are the grid voltage amplitude and angle, respectively, and ω_g is the grid frequency. In addition, in obtaining the transfer functions describing the phase and frequency estimation dynamics, it is assumed that the grid voltage amplitude V is constant.

1) Frequency Estimation Dynamics: Using Fig. 2, the differential equations describing the dynamics of the CBF-FLL2 can be obtained as

$$\dot{\hat{v}}_\alpha(t) = v'_\alpha(t) - \hat{\omega}_g \hat{v}_\beta(t) \tag{4}$$

$$\dot{\hat{v}}_\beta(t) = v'_\beta(t) + \hat{\omega}_g \hat{v}_\alpha(t) \tag{5}$$

$$\dot{v}'_\alpha(t) = -a_1 v'_\alpha(t) - \hat{\omega}_g v'_\beta(t) + a_2 v_\alpha(t) - a_2 \hat{v}_\alpha(t) \tag{6}$$

$$\dot{v}'_\beta(t) = -a_1 v'_\beta(t) + \hat{\omega}_g v'_\alpha(t) + a_2 v_\beta(t) - a_2 \hat{v}_\beta(t) \tag{7}$$

$$\dot{\hat{\omega}}_g(t) = \lambda v_q(t) = \lambda\left[v_\beta(t)\hat{v}_\alpha(t) - v_\alpha(t)\hat{v}_\beta(t)\right]. \tag{8}$$

$$G_{\text{LPF}}(s) = \frac{a_n}{s^n + a_1 s^{n-1} + a_2 s^{n-2} + \cdots + a_{n-1}s + a_n} \tag{1}$$

$$G_{\text{CBF}}(s) = G_{\text{LPF}}(s - j\omega_g) = \frac{a_n}{(s-j\omega_g)^n + a_1(s-j\omega_g)^{n-1} + a_2(s-j\omega_g)^{n-2} + \cdots + a_{n-1}(s-j\omega_g) + a_n} \tag{2}$$

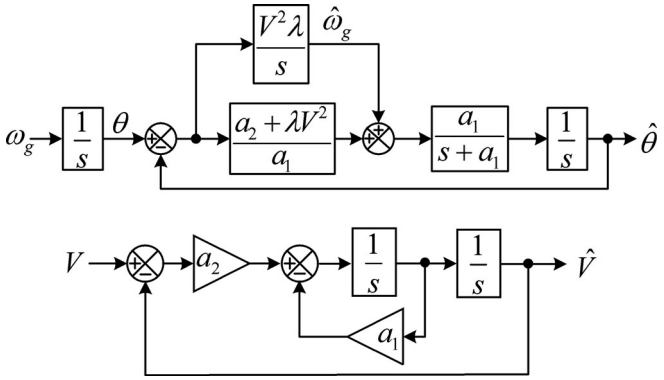

Fig. 3. Small-signal model of the CBF-FLL2.

Differentiating (8) with respect to time gives

$$\ddot{\hat{\omega}}_g = \lambda\Big[\dot{v}_\beta(t)\hat{v}_\alpha(t) + v_\beta(t)\dot{\hat{v}}_\alpha(t) - \dot{v}_\alpha(t)\hat{v}_\beta(t) - v_\alpha(t)\dot{\hat{v}}_\beta(t)\Big]. \tag{9}$$

Substituting $\dot{v}_\beta(t) = \omega_g v_\alpha(t)$, $\dot{v}_\alpha(t) = -\omega_g v_\beta(t)$, (4), and (5) into (9) yields

$$\ddot{\hat{\omega}}_g = \lambda\left[(\omega_g - \hat{\omega}_g)\underbrace{\{v_\alpha(t)\hat{v}_\alpha(t) + v_\beta(t)\hat{v}_\beta(t)\}}_{\approx V^2} + \underbrace{\{v_\beta(t)v'_\alpha(t) - v_\alpha(t)v'_\beta(t)\}}_{v'_q}\right]. \tag{10}$$

Differentiating (10) with respect to time gives

$$\dddot{\hat{\omega}}_g \approx \lambda\left[(\dot{\omega}_g - \dot{\hat{\omega}}_g)V^2 - a_1 v'_q - a_2 v_q\right]. \tag{11}$$

Considering v_q and v'_q definitions in (8) and (10), (11) can be rewritten as

$$\dddot{\hat{\omega}}_g \approx \lambda\Big[(\dot{\omega}_g - \dot{\hat{\omega}}_g)V^2 + a_1\Big\{(\omega_g - \hat{\omega}_g)V^2 - \ddot{\hat{\omega}}_g/\lambda\Big\} - a_2\dot{\hat{\omega}}_g/\lambda\Big] \tag{12}$$

or equivalently

$$\dddot{\hat{\omega}}_g + a_1\ddot{\hat{\omega}}_g + (a_2 + \lambda V^2)\dot{\hat{\omega}}_g + a_1\lambda V^2\hat{\omega}_g \approx \lambda V^2\left[\dot{\omega}_g + a_1\omega_g\right]. \tag{13}$$

Taking the Laplace transform of both sides of (13) gives

$$\hat{\omega}_g(s) \approx \frac{\lambda V^2(s + a_1)}{s^3 + a_1 s^2 + (a_2 + \lambda V^2)s + a_1\lambda V^2}\omega_g(s). \tag{14}$$

2) Phase Estimation Dynamics: Using Fig. 2, the phase angle estimated by the CBF-FLL2 can be expressed as

$$\hat{\theta} = \tan^{-1}\left(\frac{\hat{v}_\beta(t)}{\hat{v}_\alpha(t)}\right). \tag{15}$$

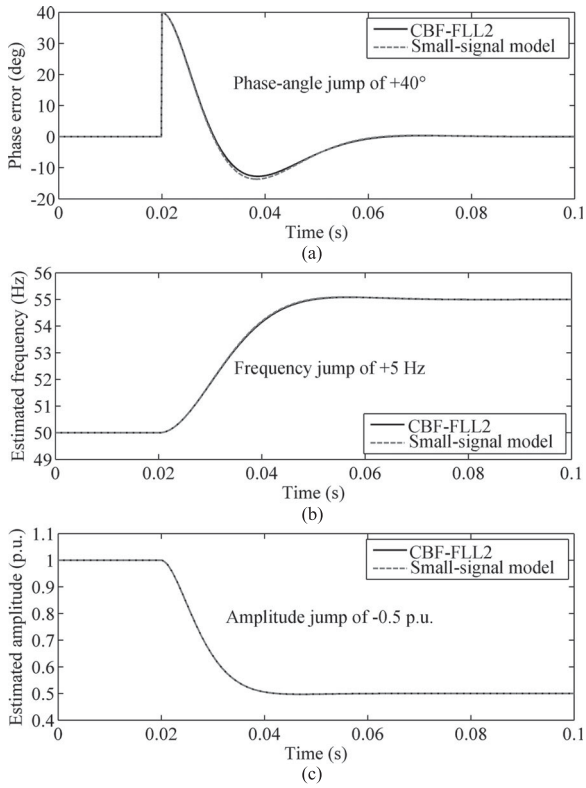

Fig. 4. Accuracy assessment of the small-signal model of the CBF-FLL2 under (a) a $+40°$ phase-angle jump, (b) $+5$ Hz frequency jump, and (c) -0.5 p.u. amplitude jump. Parameters: $a_1 = 379$, $a_2 = 49\,348$, and $\lambda = 10\,220$.

Two successive differentiations of (15) with respect to time result in

$$\dot{\hat{\theta}} = \frac{\dot{\hat{v}}_\beta(t)\hat{v}_\alpha(t) - \dot{\hat{v}}_\alpha(t)\hat{v}_\beta(t)}{\hat{v}_\alpha^2(t) + \hat{v}_\beta^2(t)} \approx \hat{\omega}_g + \frac{v'_\beta(t)\hat{v}_\alpha(t) - v'_\alpha(t)\hat{v}_\beta(t)}{V^2} \tag{16}$$

$$\ddot{\hat{\theta}} \approx \dot{\hat{\omega}}_g + \frac{a_2\overbrace{\left[v_\beta(t)\hat{v}_\alpha(t) - v_\alpha(t)\hat{v}_\beta(t)\right]}^{\dot{\hat{\omega}}_g/\lambda}}{V^2} - \frac{a_1\overbrace{\left[v'_\beta(t)\hat{v}_\alpha(t) - v'_\alpha(t)\hat{v}_\beta(t)\right]}^{V^2(\dot{\hat{\theta}} - \hat{\omega}_g)}}{V^2} = \left(\frac{\lambda V^2 + a_2}{\lambda V^2}\right)\dot{\hat{\omega}}_g + a_1\hat{\omega}_g - a_1\dot{\hat{\theta}}. \tag{17}$$

Taking the Laplace transform of both sides of (17) yields

$$\hat{\theta}(s) \approx \frac{(\lambda V^2 + a_2)s + a_1\lambda V^2}{\lambda V^2 s(s + a_1)}\hat{\omega}_g(s). \tag{18}$$

Substituting (14) into (18) with considering that $\omega_g(s) = s\theta(s)$ results in

$$\hat{\theta}(s) = \frac{(\lambda V^2 + a_2)s + a_1\lambda V^2}{s^3 + a_1 s^2 + (a_2 + \lambda V^2)s + a_1\lambda V^2}\theta(s). \tag{19}$$

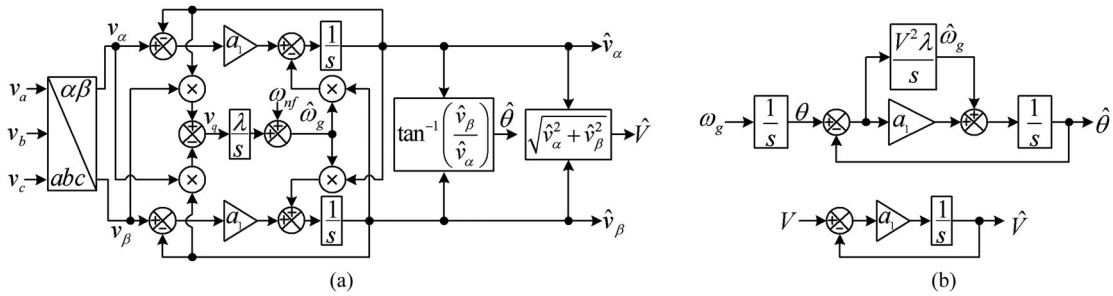

Fig. 5. (a) Schematic diagram of the CBF-FLL1 and (b) its small-signal model.

TABLE I
CONTROL PARAMETERS

	CBF-FLL2	CBF-FLL1
λ	10 220	15 791
a_1	379	177.7
a_2	49 348	—

3) Amplitude Estimation Dynamics: Based on Fig. 2, the amplitude estimated by the CBF-FLL2 can be expressed as

$$\hat{V} = \sqrt{\hat{v}_\alpha^2(t) + \hat{v}_\beta^2(t)}. \tag{20}$$

Using a similar procedure as before [i.e., successive differentiations from (20)], it can be shown that the amplitude estimation dynamics can be approximated by

$$\hat{V}(s) \approx \frac{a_2}{s^2 + a_1 s + a_2} V(s). \tag{21}$$

Based on (14), (19), and (21), the model shown in Fig. 3 can be derived for the CBF-FLL2.

4) Model Accuracy Assessment: To evaluate the accuracy of the derived model, the CBF-FLL2 and the model are both implemented in the MATLAB/Simulink environment, and their results under a phase-angle jump, frequency step change, and amplitude step variation are obtained and compared together. Fig. 4 shows the results of this comparison. As can be seen, the model accurately predicts the dynamic behavior of the CBF-FLL2, which confirms the model accuracy.

B. Stability Analysis and Tuning Control Parameters

The stability range of control parameters can be obtained by applying the Routh–Hurwitz's stability criterion to the characteristic polynomials of the CBF-FLL2 which, according to (14), (19), and (21), are $s^3 + a_1 s^2 + (a_2 + \lambda V^2)s + a_1 \lambda V^2 = 0$ and $s^2 + a_1 s + a_2 = 0$. The obtained results indicate that the CBF-FLL2 will be stable if $a_1 > 0$, $a_2 > 0$, and $\lambda > 0$.

In the tuning procedure, the focus is on the phase loop dynamics and stability margin. The reason is that, from the amplitude and frequency estimation points of view, the FLL is a type-1 control system. However, from the phase-angle estimation point of view, it is a type-2 control system. It is well-known that the stability problem is aggravated by increasing the type of the control system.

Using Fig. 3, the phase estimation open-loop transfer function can be obtained as

$$G_{ol}(s) = \frac{\hat{\theta}(s)}{\theta(s) - \hat{\theta}(s)} = \frac{k_1(s + z_1)}{s^2(s + a_1)} \tag{22}$$

where $z_1 = \frac{a_1 \lambda V^2}{a_2 + \lambda V^2}$ and $k_1 = a_2 + \lambda V^2$. Applying the symmetrical optimum design method [12] to (22) determines k_1, z_1, and a_1 as

$$\begin{aligned} k_1 &= b\omega_c^2 \\ z_1 &= \omega_c / b \\ a_1 &= b\omega_c \end{aligned} \tag{23}$$

where ω_c is the crossover frequency (the frequency at which the open-loop magnitude-frequency response crosses 0 dB) and b is a design constant that determines the phase margin (PM) as $\text{PM} = \tan^{-1}(\frac{b^2 - 1}{2b})$. Considering k_1 and z_1 definitions and (23), it is easy to obtain

$$\begin{aligned} a_1 &= b\omega_c \\ a_2 &= (b - 1/b)\omega_c^2 \\ \lambda &= \frac{\omega_c^2}{bV^2}. \end{aligned} \tag{24}$$

Now, the control parameters a_1, a_2, and λ can be determined by selecting appropriate values for the crossover frequency ω_c and the design constant b. Here, as recommended in [12], $b = 1 + \sqrt{2}$ is selected. This value is corresponding to a PM of 45°, which ensures a sufficient stability margin and a satisfactory compromise between the speed of response and overshoot. Regarding the crossover frequency ω_c, the selection involves a tradeoff between the disturbance rejection capability and the speed of response. Here, to achieve a satisfactory compromise, $\omega_c = 2\pi 25$ rad/s is chosen. The selected values for b and ω_c determine the control parameters of the CBF-FLL2 as $a_1 = 379$, $a_2 = 49\,348$, and $\lambda = 10\,220$.

IV. ANALYSIS

In this section, a theoretical performance comparison between the CBF-FLL2 and a first-order CBF-based FLL (CBF-FLL1)

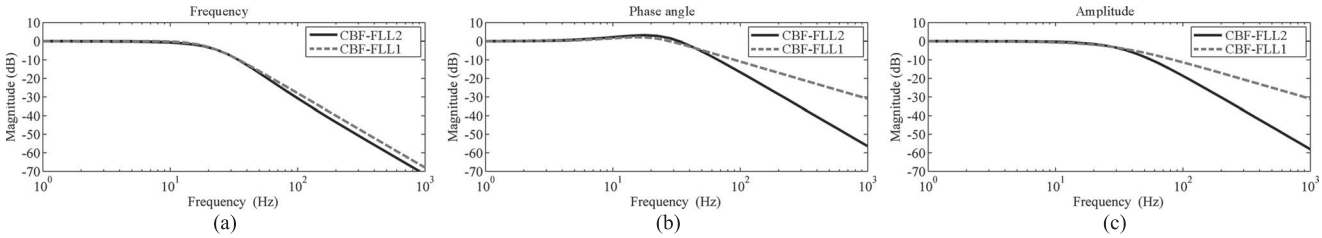

Fig. 6. Closed-loop magnitude frequency response of the CBF-FLL2 and the CBF-FLL1 in the estimation of (a) frequency, (b) phase angle, and (c) amplitude.

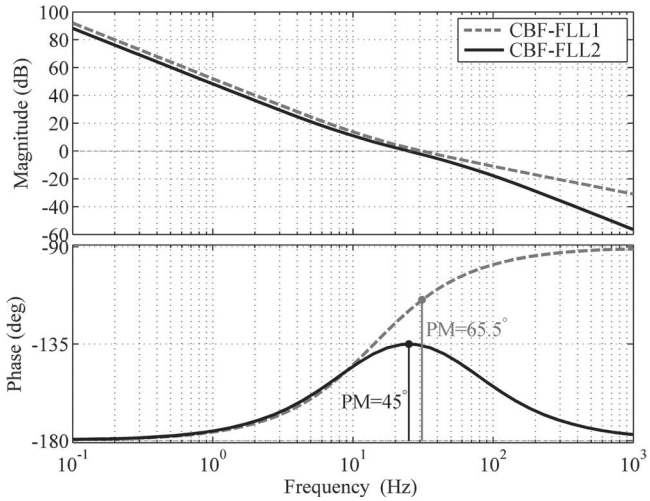

Fig. 7. Phase estimation open-loop Bode plots for the CBF-FLL2 and the CBF-FLL1.

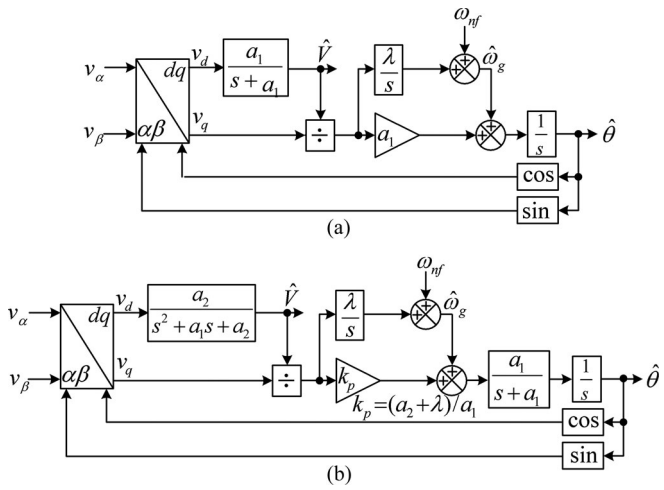

Fig. 8. Equivalent PLL structures to (a) the CBF-FLL1 and (b) CBF-FLL2.

is conducted. A unification between FLLs and PLLs is also provided here.

The schematic diagram of the CBF-FLL1 can be observed in Fig. 5(a). Based on this structure and following a similar procedure as that described for the CBF-FLL2, the characteristic transfer functions of the CBF-FLL1 can be derived as

$$\hat{\theta}(s) \approx \frac{a_1 s + \lambda V^2}{s^2 + a_1 s + \lambda V^2}\theta(s) \tag{25}$$

$$\hat{\omega}(s) \approx \frac{\lambda V^2}{s^2 + a_1 s + \lambda V^2}\omega(s) \tag{26}$$

$$\hat{V}(s) \approx \frac{a_1}{s + a_1}V(s). \tag{27}$$

Based on these transfer functions, the CBF-FLL1 model can be derived, as shown in Fig. 5(b). Notice that, in obtaining (25) and (26), the grid voltage amplitude V is considered to be a constant.

The control parameters of the CBF-FLL1 can be selected using the standard design approach for second-order systems, i.e., defining $a_1 = 2\zeta\omega_n$ and $\lambda = (\omega_n/V)^2$ and selecting proper values for the natural frequency ω_n and the damping factor ζ. Here, $\zeta = 1/\sqrt{2}$ and $\omega_n = 2\pi 20$ rad/s are considered. These values ensure an optimum damping and almost the same closed-loop bandwidth as that of the CBF-FLL2. These selected values result in $a_1 = 177.7$ and $\lambda = 15791$. Table I summarizes the control parameters of both the CBF-FLL2 and the CBF-FLL1.

Fig. 6 illustrates the closed-loop magnitude–frequency response of the CBF-FLL2 and the CBF-FLL1 in the estimation of grid voltage frequency, phase angle, and amplitude. It can be observed that the CBF-FLL2 provides a higher attenuation rate in the estimation of grid voltage phase angle and amplitude than the CBF-FLL1, which implies that it provides a higher filtering capability in the estimation of these quantities. In the estimation of grid frequency, however, both FLLs have the same roll-off speed and, therefore, a close disturbance rejection capability.

Fig. 7 shows the phase estimation open-loop Bode plots for the CBF-FLL2 and the CBF-FLL1. It can be observed that the CBF-FLL1 offers a higher PM than the CBF-FLL2, which implies that it has a lower overshoot peak during phase-angle jumps. This result was expected because there is a first-order LPF in the forward path of the CBF-FLL2 model [see Fig. 3], which causes an additional in-loop phase delay and, therefore, degrades the PM.

A. Unification Between FLLs and PLLs

Based on the characteristic transfer functions and models derived for the CBF-FLL1 and the CBF-FLL2, it can be proved that they are mathematically equivalent to the PLL structures shown in Fig. 8. A hidden assumption here is that the CBF-FLL1 and the CBF-FLL2 use an amplitude normalization

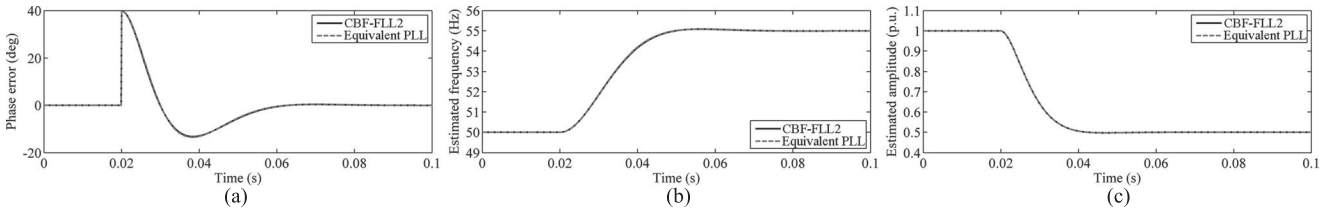

Fig. 9. Performance comparison between the CBF-FLL2 and its PLL counterpart under (a) a phase-angle jump of $+40°$, (b) a frequency jump of $+5$ Hz, and (c) a symmetrical voltage sag of 0.5 p.u.

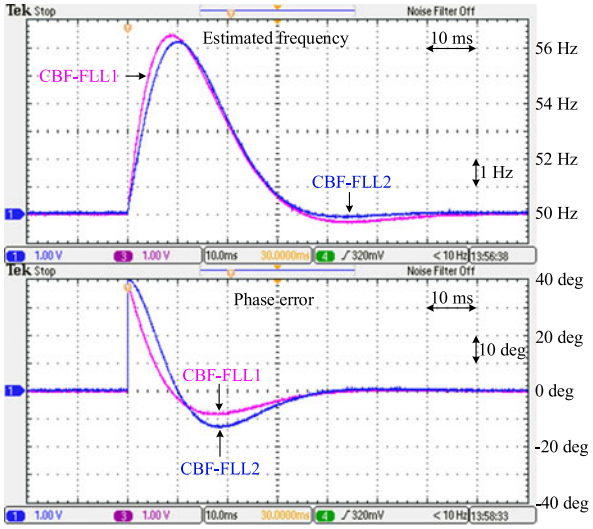

Fig. 10. Experimental results for test case 1.

scheme in their structures. To verify this equivalence, Fig. 9 compares the performance of the CBF-FLL2 and its PLL counterpart under the same tests used for the model accuracy assessment (see Fig. 4). The obtained results confirm the equivalence. Roughly speaking, this equivalence implies that PLLs and FLLs are the same systems that are implemented in different reference frames.

V. Experimental Results

In this section, a comparative performance evaluation between the CBF-FLL2 and the CBF-FLL1 is carried out. In obtaining all results, the sampling frequency and the nominal grid frequency are considered to be 10 kHz and 50 Hz, respectively. All experimental results are obtained using dSPACE 1006 platform. The parameters summarized in Table I are considered for obtaining the experimental results. To make the performance of both FLLs insensitive to the grid voltage amplitude variation, an amplitude normalization technique is included into their structures.

Three test cases are designed.

1) *Test case 1:* The grid voltage experiences a phase-angle jump of $+40°$.
2) *Test case 2:* The grid voltage is harmonically distorted. The grid voltage components in this test are $V_1^+ = 1$ p.u., $V_5^- = 0.1$ p.u., $V_7^+ = 0.1$ p.u., $V_{11}^- = 0.05$ p.u., and $V_{13}^+ = 0.05$ p.u.

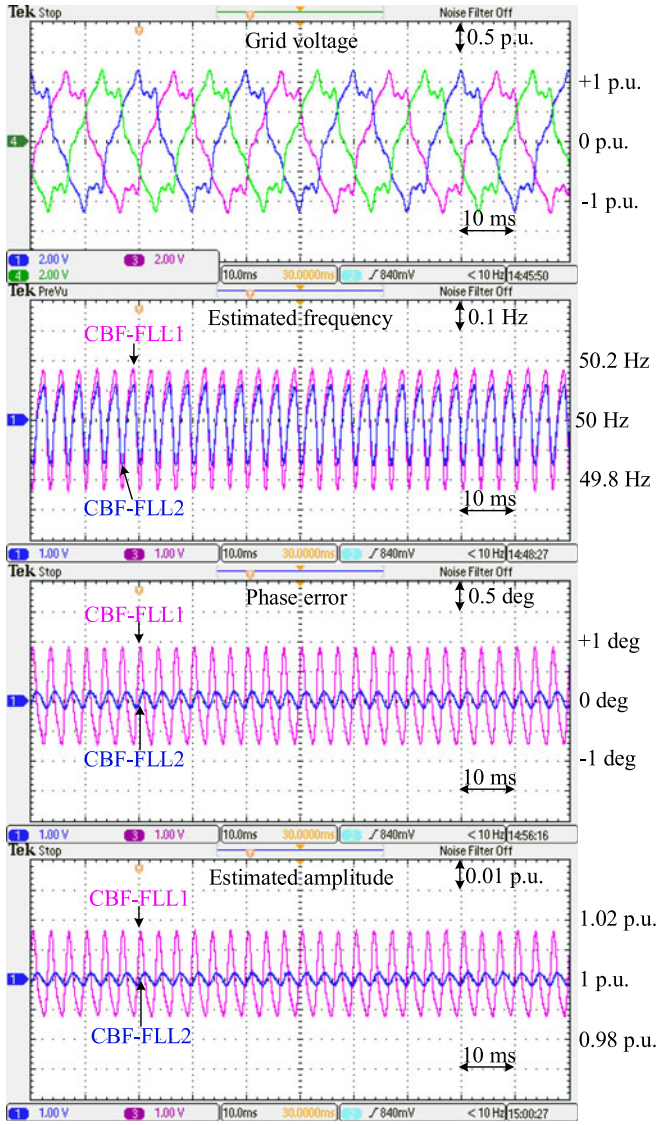

Fig. 11. Experimental results for test case 2.

3) *Test case 3:* The grid voltage first undergoes a symmetrical voltage sag of 0.25 p.u. Then, a single-phase voltage sag of 0.75 p.u. in the phase A happens.

Fig. 10 shows the obtained results for test case 1. Both FLLs have a close settling time, which is around two cycles of the nominal frequency. A noticeable difference in this test is the lower peak phase error of the CBF-FLL1, which, as explained before, is because of its higher PM.

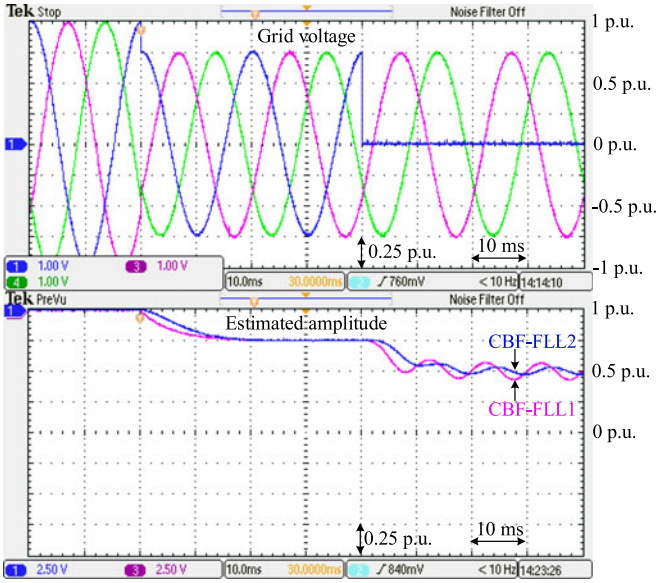

Fig. 12. Experimental results for test case 3.

The experimental results for test case 2 are shown in Fig. 11. It can be observed that the CBF-FLL2 provides a much higher filtering capability in the phase and amplitude estimation than the CBF-FLL1. However, in the estimation of the frequency, there is not a large difference between them. These results were predicted before (see Fig. 6).

Fig. 12 illustrates the obtained results for test case 3. From the transient response point of view, both FLLs provide a close performance. The CBF-FLL2, however, offers a higher imbalance rejection capability in the amplitude estimation. This fact is noticeable from lower double-frequency oscillatory errors in the amplitude estimated by the CBF-FLL2.

VI. Conclusion

The critical analysis of high-order FLLs was the main aim of this letter. To this end, a general approach for designing high-order FLLs for three-phase systems was first proposed. Then, the CBF-FLL2 was considered as the case study, and its small-signal modeling, stability analysis, and tuning were presented. By considering the CBF-FLL1 as the base for comparison, it was discussed theoretically and verified experimentally that the CBF-FLL2 can provide a considerably higher filtering capability in the estimation of grid voltage phase and amplitude. However, it is not able to do so in the case of frequency estimation. It was also shown that the CBF-FLL2 has a lower stability margin than the CBF-FLL1. Finally, an equivalence between FLLs and PLLs demonstrated. Roughly speaking, this equivalence implies that PLLs and FLLs are the same systems that are implemented in different reference frames.

References

[1] S. Golestan, M. Ramezani, J. M. Guerrero, F. D. Freijedo, and M. Monfared, "Moving average filter based phase-locked loops: Performance analysis and design guidelines," *IEEE Trans. Power Electron.*, vol. 29, no. 6, pp. 2750–2763, Jun. 2014.

[2] S. Golestan, J. M. Guerrero, and J. C. Vasquez, "Three-phase PLLs: A review of recent advances," *IEEE Trans. Power Electron.*, vol. 32, no. 3, Mar. 2017.

[3] P. Rodriguez, A. Luna, I. Candela, R. Mujal, R. Teodorescu, and F. Blaabjerg, "Multiresonant frequency-locked loop for grid synchronization of power converters under distorted grid conditions," *IEEE Trans. Ind. Electron.*, vol. 58, no. 1, pp. 127–138, Jan. 2011.

[4] J. Matas, M. Castilla, J. Miret, L. G. Vicuna, and R. Guzman, "An adaptive prefiltering method to improve the speed/accuracy tradeoff of voltage sequence detection methods under adverse grid conditions," *IEEE Trans. Ind. Electron.*, vol. 61, no. 5, pp. 2139–2151, May 2014.

[5] Z. Xin, X. Wang, Z. Qin, M. Lu, P. C. Loh, and F. Blaabjerg, "An improved second-order generalized integrator based quadrature signal generator," *IEEE Trans. Power Electron.*, vol. 31, no. 12, pp. 8068–8073, Dec. 2016.

[6] S. Vazquez, J. Sanchez, M. Reyes, J. Leon, and J. Carrasco, "Adaptive vectorial filter for grid synchronization of power converters under unbalanced and/or distorted grid conditions," *IEEE Trans. Ind. Electron.*, vol. 61, no. 3, pp. 1355–1367, Mar. 2014.

[7] M. Karimi Ghartemani, *Enhanced phase-locked loop structures for power and energy applications*. New York, NY, USA: Wiley-IEEE Press, 2014.

[8] X. Guo and W. Y. Wu, "Simple synchronisation technique for three-phase grid-connected distributed generation systems," *IET Renew. Power Gener.*, vol. 7, no. 1, pp. 55–62, Jan. 2013.

[9] Z. Xin, R. Zhao, P. Mattavelli, P. C. Loh, and F. Blaabjerg, "Reinvestigation of generalized integrator based filters from a first-order-system perspective," *IEEE Access*, vol. 4, pp. 7131–7144, 2016.

[10] M. H. Bollen and G. Irene, *Signal Processing of Power Quality Disturbances.* New York, NY, USA: Wiley, 2006.

[11] M. Illindala and G. Venkataramanan, "Frequency/sequence selective filters for power quality improvement in a microgrid," *IEEE Trans. Smart Grid*, vol. 3, no. 4, pp. 2039–2047, Dec. 2012.

[12] S. Golestan, M. Monfared, and F. D. Freijedo, "Design-oriented study of advanced synchronous reference frame phase-locked loops," *IEEE Trans. Power Electron.*, vol. 28, no. 2, pp. 765–778, Feb. 2013.